PASJ: Publ. Astron. Soc. Japan **57**, 595–603, 2005 August 25

Multi-Epoch VERA Observations of H_2O Masers in OH 43.8−0.1

Mareki HONMA,[1,2] Takeshi BUSHIMATA,[1,3] Yoon Kyung CHOI,[1,4] Takahiro FUJII,[1,5] Tomoya HIROTA,[1] Koji HORIAI,[1,6] Hiroshi IMAI,[5] Noritomo INOMATA,[5] Jose ISHITSUKA,[1] Kenzaburo IWADATE,[1,6] Takaaki JIKE,[1] Osamu KAMEYA,[1,2,6] Ryuichi KAMOHARA,[1,5] Yukitoshi KAN-YA,[1] Noriyuki KAWAGUCHI,[1,2,3] Masachika KIJIMA,[5] Hideyuki KOBAYASHI,[1,3,4] Seisuke KUJI,[1,6] Tomoharu KURAYAMA,[1,4] Seiji MANABE,[1,2,6] Takeshi MIYAJI,[1,3] Akiharu NAKAGAWA,[5] Kouichirou NAKASHIMA,[5] Chung Sik OH,[1,4] Toshihiro OMODAKA,[5] Tomoaki OYAMA,[1,4] Maria RIOJA,[7] Satoshi SAKAI,[1,6] Katsuhisa SATO,[1,6] Tetsuo SASAO,[8] Katsunori M. SHIBATA,[1,3] Rie SHIMIZU,[5] Kasumi SORA,[5] Hiroshi SUDA,[1,4] Yoshiaki TAMURA,[1,2,6] and Kazuyoshi YAMASHITA[5]

[1]*VERA Observatory, NAOJ, Mitaka, Tokyo 181-8588*
[2]*Graduate University for Advanced Studies, Mitaka, Tokyo 181-8588*
[3]*Space VLBI Project, NAOJ, Mitaka, Tokyo 181-8588*
[4]*Department of Astronomy, The University of Tokyo, Bunkyo-ku, Tokyo 113-8654*
[5]*Faculty of Science, Kagoshima University, Korimoto, Kagoshima, Kagoshima 890-0065*
[6]*Mizusawa Astrogeodynamics Observatory, NAOJ, Mizusawa, Iwate 023-0861*
[7]*Observatorio Astronómico Nacional, Madrid, Spain*
[8]*Ajou University, Suwon 443-749, Republic of Korea*
honmamr@cc.nao.ac.jp

(Received 2005 February 15; accepted 2005 May 4)

Abstract

We report on multi-epoch observations of H_2O maser emission in the star-forming region OH 43.8−0.1, carried out with VLBI Exploration of Radio Astrometry. The large-scale maser distributions obtained by single-beam VLBI mapping reveal new maser spots scattered over the area of $0\farcs7 \times 1\farcs0$, in addition to a 'shell-like' structure with a scale of $0\farcs3 \times 0\farcs5$, which was mapped previously. Proper motions were also obtained for 43 spots based on 5-epoch monitoring with a time span of 281 days. The distributions of the proper motions show a systematic outflow in the north–south direction with an expansion velocity of $\sim 8\,\mathrm{km\,s^{-1}}$. The overall distributions of the maser spots as well as the proper motions are better represented by a bipolar flow plus a central maser cluster with a complex structure, rather than a shell with uniform expansion, such as those found in Cep A R5 and W 75N VLA2. The distance to OH 43.8−0.1 was also estimated based on the statistical parallax, yielding $D = 2.8 \pm 0.5\,\mathrm{kpc}$. This distance is consistent with a near kinematic distance, and rules out a far kinematic distance ($\sim 9\,\mathrm{kpc}$). Also, the radial velocity of the OH 43.8−0.1 combined with the distance provides a constraint on the flatness of the galactic rotation curve, indicating that there is no systematic difference in the rotation speeds at the Sun and at the position of OH 43.8−0.1, which is located at a galacto-centric radius of $\sim 6.3\,\mathrm{kpc}$.

Key words: Galaxy: kinematics and dynamics — ISM: H II regions — ISM: individual (OH 43.8−0.1) — masers (H_2O)

1. Introduction

Star-forming regions are often associated with water maser emission, and multi-epoch VLBI observations of water masers provide a unique tool to study the structure and kinematics of star-forming regions through the proper motions of maser spots. Until the middle of the 1990s, VLBI studies of H_2O maser sources were made to reveal the kinematics in well-known star-forming regions, such as Orion KL, W 51M and N, Sgr B2, W 49N, and W 3(OH) (Genzel et al. 1981a, 1981b; Schneps et al. 1981; Reid et al. 1988; Gwinn et al. 1992; Alcolea et al. 1993). These studies successfully detected the proper motions of maser spots, and demonstrated that maser emitting gases trace the shock regions where the outflows from forming stars hit ambient gases. The proper motions of maser spots were also used to determine the source distance via statistical parallax and/or detailed kinematic modeling, providing a powerful tool to determine distances on the galactic scale, even up to $\sim 10\,\mathrm{kpc}$. Recently, numerous efforts were made to perform VLBI studies of a greater number of star-forming regions, and detected proper motions of H_2O masers in several other sources, such as IRAS 05413−0104, IRAS 21391+5802, S 106 FIR, W 3 IRS5, W 51S, Cep A, W 75N, NGC 2071, AFGL 5142, IRAS 20050+2720 (e.g., Claussen et al. 1998; Patel et al. 2000; Furuya et al. 2000; Imai et al. 2000, 2002; Torrelles et al. 2001, 2003; Seth et al. 2002; Goddi et al. 2004; Furuya et al. 2005). While most H_2O maser sources show bipolarity in their distributions as well as motions, there are a few exceptions that exhibit a coherently expanding shell (Cep A R5 and W 75N VLA2: Torrelles et al. 2001, 2003), casting a question about the formation mechanism of these morphologically different outflows in star-forming regions.

OH 43.8−0.1 (also referred to as G43.8−0.1 or G43.795−0.127) is a star-forming region located in the

galactic plane with OH, CH_3OH, and H_2O maser emissions. While optical and near IR observations tell little about this region due to the extremely large galactic extinction, this star-forming region is known to be associated with an infrared source, IRAS 19095+0930, and an Ultra-Compact H II region (hereafter UC H II, Kurtz et al. 1994). VLA studies of OH maser distributions revealed that OH maser spots surround UC H II (Argon et al. 2000). Molecular lines, such as CO and CS, were also detected toward the direction of OH 43.8−0.1 (Plume et al. 1992; Shepherd, Churchwell 1996), providing a radial velocity with respect to the Local Standard of Rest as $V_{\rm LSR} \sim 44\,{\rm km\,s^{-1}}$. Assuming the standard galactic rotation (a flat rotation curve with $R_0 = 8.5\,{\rm kpc}$ and $\Theta_0 = 220\,{\rm km\,s^{-1}}$), the systemic velocity gives a near-kinematic distance of 3 kpc and a far distance of 9 kpc. H_2O maser emission in OH 43.8−0.1 was discovered by Genzel and Downes (1977) and Dickinson et al. (1978), and shortly later VLBI observations of H_2O masers were carried out by Downes et al. (1979). The distribution of maser spots obtained by Downes et al. (1979) suggested a shell-like structure with a diameter of 0.″5. Therefore, OH 43.8−0.1 is another candidate for H_2O maser sources that show a shell-like morphology, such as those recently found in Cep A R5 and W 75N VLA2 (Torrelles et al. 2001, 2003). In order to confirm (or rule out) this, new multi-epoch VLBI observations are necessary to measure the proper motions of maser spots.

Here, we present the results of multi-epoch observations of OH 43.8−0.1 H_2O masers with VLBI Exploration of Radio Astrometry (VERA), which is a new Japanese VLBI array dedicated to phase-referencing VLBI astrometry (Honma et al. 2000; Kobayashi et al. 2003). Originally, the observations of OH 43.8−0.1 were carried out as a series of test observations to evaluate the system performance of VERA, by observing OH 43.8−0.1 and another bright maser source, W 49N, simultaneously in the dual-beam mode. The series of test observations already demonstrated a high capability of phase-referencing with VERA's dual-beam system (Honma et al. 2003), and also produced maser maps of W 49N, successfully identifying the outburst spots that flared up in 2003 October (Honma et al. 2004). In the present paper, we focus on the results concerning OH 43.8−0.1, analyzed as single-beam VLBI observations. We presented the maser spots map in larger scale than that of Downes et al. (1979), and measured the proper motions for the first time for OH 43.8−0.1 based on 5-epoch observations spanning 281 days. We also determined the distance to OH 43.8−0.1 based on statistical parallax, and analyzed the structure and kinematics of the OH 43.8−0.1 masers as well as the constraint on the galactic rotation curve obtained from the distance to OH 43.8−0.1.

2. Observations and Reductions

VERA observations of OH 43.8−0.1 were performed for 9 epochs between October in 2003 and September in 2004 with typical intervals of 1–2 months as a series of test observations of VERA. The observations were done in the dual-beam mode observing two bright H_2O maser sources, W 49N and OH 43.8−0.1 (0.°65 separation), simultaneously to evaluate the capability of phase-referencing as well as astrometric precision. The results of phase-referencing performance tests as well as the dual-beam astrometric capability will be discussed elsewhere, and we concentrate on OH 43.8−0.1 in this paper. Left-hand circular polarization signals were digitized and recorded using the VSOP-terminal system at a data rate of 128 Mbps with 2-bit quantization. Among the total bandwidth of 32 MHz, one 16 MHz channel was assigned to OH 43.8−0.1, covering the radial velocity span of $215.7\,{\rm km\,s^{-1}}$. Correlation processing was performed with the Mitaka FX correlator with a spectral resolution of 512 points per channel, yielding frequency and velocity resolutions of 31.25 kHz and $0.42\,{\rm km\,s^{-1}}$, respectively.

In some epochs, one or a few stations were partly or fully missed due to system trouble and/or bad weather. Since the VERA array has only 4 stations (Mizusawa, Iriki, Ogasawara, and Ishigaki-jima), the lack of a station causes severe degrading of synthesized images, and would introduce a large error in conducting multi-epoch measurements of maser proper motions. Hence, in the present paper, we use the data of 5 epochs that were obtained with the full 4-station array under relatively good conditions. The epochs presented here are: day of year (DOY) 356 in 2003, DOY 054, 120, 205, and 272 in 2004 (December 22 in 2003, February 23, April 29, June 23, and September 28 in 2004). The system noise temperatures at the zenith were typically 150 K to 250 K for the first three epochs, and 200 K to 300 K for the last two epochs.

In the data analysis of each epoch, calibrations of the clock parameters, bandpass, amplitude, radial velocity, and phase were carried out in a standard manner. The clock parameters (clock offset and clock rate offset) were calibrated using the residual delay and delay rate for a bright calibrator source, TXS 1923+210 (= ICRF J192559.6+210626), which was observed every two hours. Bandpass calibrations were made using auto-correlation spectra of continuum sources. The amplitude calibrations were done using the system noise temperature; they were evaluated by the 'R-Sky' method, by observing a reference black body at the beginning of each scan (typically every hour). Observed frequencies of maser lines were converted to the LSR velocities ($V_{\rm LSR}$, radial velocities with respect to the Local Standard of Rest) using a rest frequency of 22.235080 GHz for H_2O 6_{16}–5_{23} transition. For phase calibrations, the visibilities of all velocity channels were phase-referenced to the reference maser spot at a $V_{\rm LSR}$ of $38.2\,{\rm km\,s^{-1}}$, which is one of the brightest spots; it shows no sign of structure according to the closure phase. After those processes, calibrated visibilities were Fourier transformed to synthesized images, and the positions of the brightness peaks were determined with respect to the reference maser spot (note that the reference spot was the same for all epochs). The synthesized beam has a FWHM beam size of $1.2\,{\rm mas} \times 2.3\,{\rm mas}$ with a PA of 45°. In order to detect maser spots that are far from the reference spot, the spot positions were first estimated using fringe rates, and detailed mapping was performed around the estimated positions.

For analyses of multi-epoch VLBI data, we identified maser spots based on spot positions as well as radial velocities. Spots in different epochs were identified as 'same' if their positions were within 1 mas and their radial velocities were within $0.21\,{\rm km\,s^{-1}}$, which is half of the velocity resolution.

For maser spots that were detected for more than 3 epochs, their proper motions were determined based on a linear least-squares-fit.

3. Results

3.1. Spectral Evolution

Figure 1 shows the spectral evolutions of OH 43.8−0.1 for 5 epochs. The LSR velocities of the maser lines range from 25 to 54 km s^{-1}, showing no major difference from the observations in 1977 (Downes et al. 1979). As can be seen in figure 1, the auto-correlation spectra of OH 43.8−0.1 showed a rapid variability of the maser intensity during our observations. The strong variability of OH 43.8−0.1 was already found by long-term monitoring by Lekht (2000), and similar variabilities were found in many of H_2O maser sources, including the rapid flare-up of a certain feature. The most prominent variation occurred at a V_{LSR} of 38.2 km s^{-1}, which had 1.0×10^3 Jy on DOY 356 in 2003 and decreased to 75 Jy on DOY 272 in 2004. Lekht (2000) also found a rapid flare at V_{LSR} = 38.2 km s^{-1} in 1997, exceeding 3.7×10^3 Jy, with a duration of 6 months.

Figure 1 also shows the cross-correlated spectra of OH 43.8−0.1 for Mizusawa–Ishigaki-jima baseline, which is the longest among the 6 baselines of VERA. The cross-correlation spectra in figure 1 were taken around the maximum UV distance, being $\sim$ 2200 km or $1.6 \times 10^8 \lambda$. In figure 1, for some features the correlated flux is much smaller than the total power flux, indicating that the maser features are partially or fully resolved out with this baseline. The LSR velocities of cross-correlated maser lines mostly range from 34 to 51 km s^{-1}, while some features around 25 to 34 km s^{-1} were detected in the cross-correlated spectrum on DOY 120 in 2004. The component of V_{LSR} = 38.2 km s^{-1} is strongest in cross-correlated spectra in the first three epochs, with its peak intensity of 870 Jy on DOY 356 in 2003. The high ratio of the correlated flux to the total flux (8.7×10^2 Jy to 1.0×10^3 Jy) suggests that the flaring of the 38.2 km s^{-1} spot occurred in a compact area, being smaller than 6 AU (corresponding to 2 mas at a distance of 2.8 kpc; see subsection 3.4 for distance determination). As described in the previous section, the maser spot at 38.2 km s^{-1} was taken to be the reference spot for visibility phase calibrations.

3.2. Maser Spot Distributions

Figure 2a shows a composite map of OH 43.8−0.1 maser spot distributions with a size of $1\farcs5 \times 1\farcs5$. Spots that were detected at least in one epoch are plotted. The number of detected maser spots in each epoch are 53, 54, 60, 47, and 51 from DOY 356 in 2003 to DOY 272 in 2004. For maser spots detected for more than 3 epochs, the proper-motion vectors are superposed (for proper motion measurements, see next subsection).

The map origin of figure 2a is the position of the reference maser spot at V_{LSR} = 38.2 km s^{-1}. The absolute position of the map origin is estimated to be (α_{J2000}, δ_{J2000}) = ($19^h11^m53\fs986$, $+09°35'50\farcs22$) with an uncertainty of $0\farcs2$ using the fringe rates of the reference maser spot. The color index in figure 2 shows the LSR velocity range from 34.4 km s^{-1} to 50.9 km s^{-1}, where most of maser spots are located. The only exceptions are those with LSR velocities of 25–34 km s^{-1}, which were only detected on DOY 120 of 2004, and are shown as open circles in figure 2b and 2c.

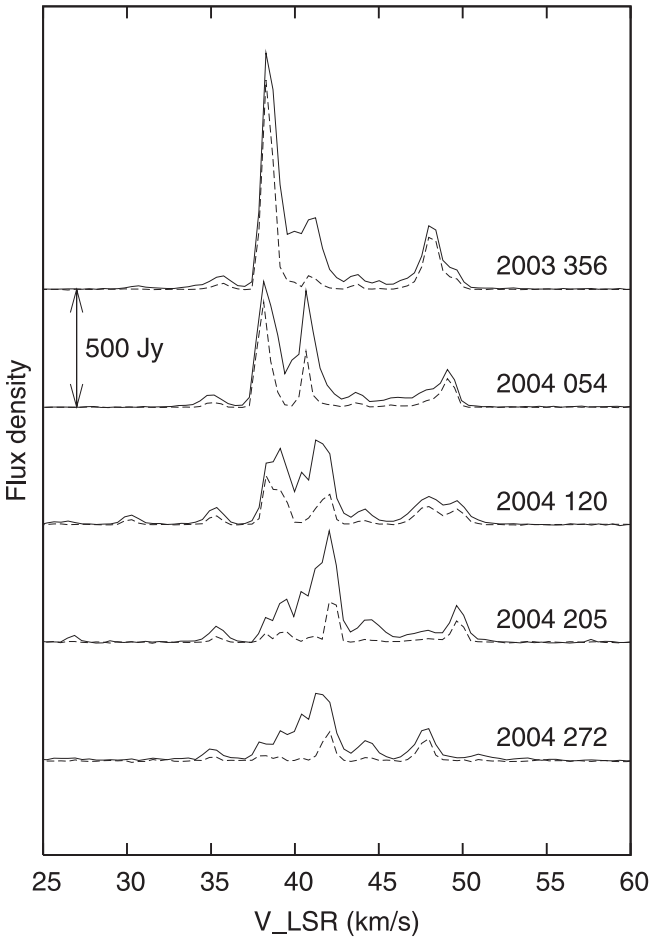

Fig. 1. Five-epoch spectral evolution of OH 43.8−0.1 H_2O masers. The thin lines show the total flux (auto-correlation), and the dashed lines show the cross-correlated flux for the Mizusawa–Ishigaki-jima baseline. The vertical arrow shows the flux scale of 500 Jy, and each spectrum is displaced by the same amount.

Figure 2b is an expanded map of the shell-like structure, which was originally discovered by Downes et al. (1979). While figure 2b is consistent with the map obtained by Downes et al., figure 2a shows that the shell-like structure found previously does not represent the entire region of the maser spot distributions. In fact, in figure 2a, the maser distributions show an extension with a scale of $\sim 1''$ from the northern top of a shell-like structure toward the south. This extension of maser spots was not reported in previous studies, and was discovered for the first time in the present study. The northern maser spots around (−145, 136) have V_{LSR} values of 47 to 51 km s^{-1}, and the southern-most maser spot at (129, −810) has a V_{LSR} of 41 km s^{-1}. These properties of the spot positions as well as the radial velocities indicate that the maser spot distribution in OH 43.8−0.1 is not represented by a simple shell, but may be interpreted as a bipolar structure in the north–south direction. In addition to the north–south extension, there are a few other maser spots that are rather isolated, such as the ones at

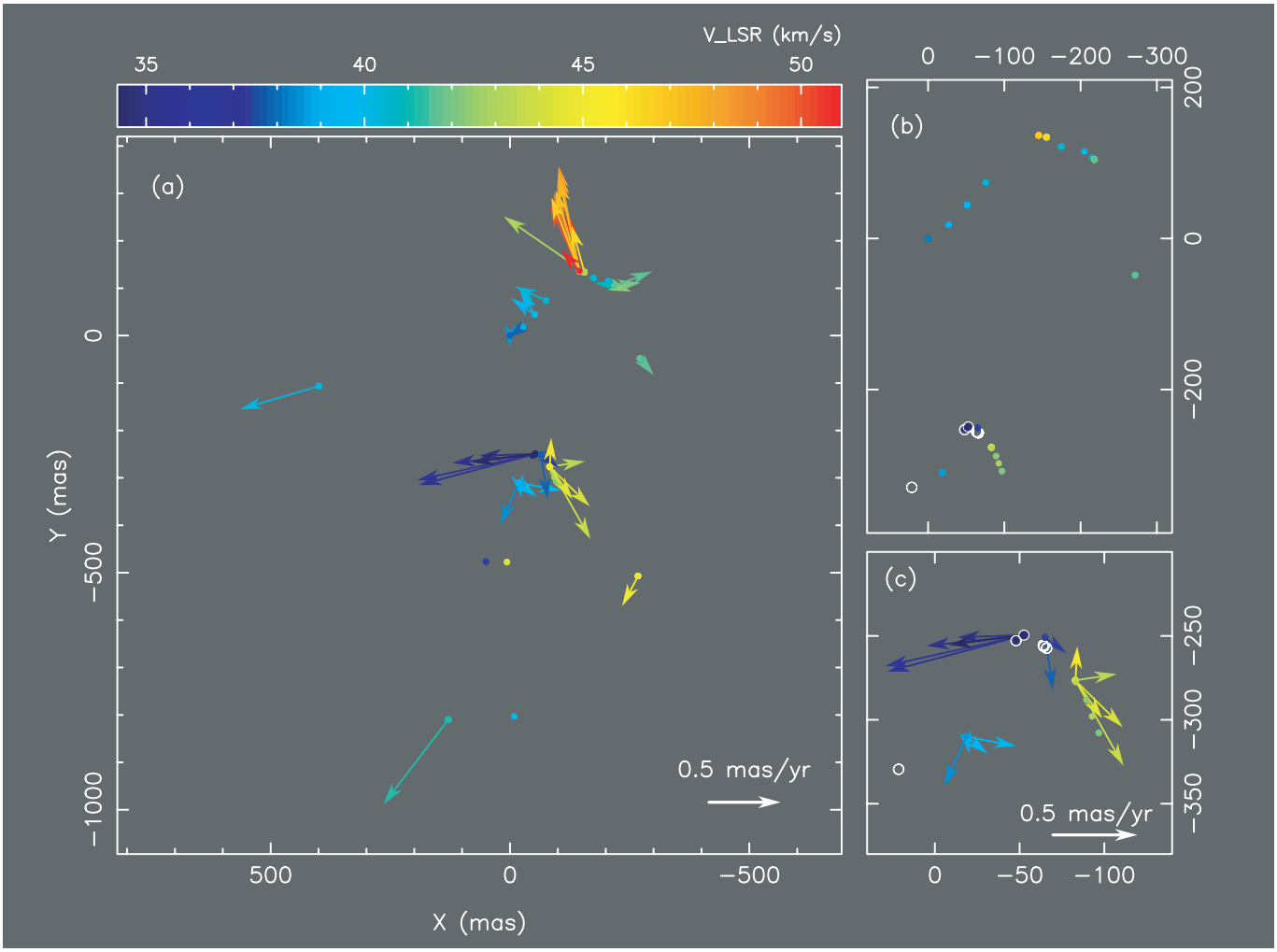

Fig. 2. Composite map of maser spot distributions and proper motion vectors of OH 43.8−0.1. The spot color indicates the LSR velocity (see color index at the top). The systemic velocity of OH 43.8−0.1 is $V_{\rm LSR} \approx 42\,{\rm km\,s^{-1}}$. Left (a) Large-scale map with a size of $1\farcs5 \times 1\farcs5$ ($1''$ corresponds to 2800 AU at a distance of 2.8 kpc). The arrow at the bottom-right corner indicates a proper motion of $0.5\,{\rm mas\,yr^{-1}}$, corresponding to $6.6\,{\rm km\,s^{-1}}$ at a distance of 2.8 kpc. Top-right (b) Expansion of the shell-like structure found by Downes et al. (1979). Bottom-right (c) Close-up to the central cluster with proper-motion vectors. The circles in (b) and (c) are maser spots with LSR velocities out of the color index range ($V_{\rm LSR} = 25$ to $34\,{\rm km\,s^{-1}}$), detected only in DOY 120 of 2004.

$(X, Y) = (399, -107)$ and $(-268, -507)$, which were also not reported in previous studies.

3.3. *Proper Motion Measurements*

As described in the previous section, maser spots in different epochs were identified as 'same' if their positions and velocities were within 1 mas and $0.21\,{\rm km\,s^{-1}}$, respectively. Based on these identification criteria, 43 maser spots were identified in more than 3 epochs, and the proper motions were determined based on a linear least-squares-fit. Table 1 summarizes the results of proper-motion measurements obtained by a linear least-squares-fit, including LSR velocities, spot positions, proper motions, detected epochs, and RMS residuals. Note that the RMS residuals, δ_X and δ_Y, are defined as $\delta_X = \sqrt{\sum (X_{\rm obs} - X_{\rm fit})^2 / n}$, where $X_{\rm obs}$ and $X_{\rm fit}$ are the observed and best-fit positions of spots and n is the number of data ($3 \leq n \leq 5$). The values of δ_X and δ_Y provide uncertainty estimates of the proper-motion measurements. The maximum values of δ_X and δ_Y are 0.060 and 0.082 mas, and the mean values of δ_X and δ_Y for 43 spots are 0.022 and 0.029 mas. These values indicate that the proper-motion measurements were successfully done with an accuracy of better than 0.1 mas. Also, in table 1 there is no systematic trend in δ_X and δ_Y with the LSR velocity or position of the maser spots. Since the maser spots are bright enough (typically larger than 10 Jy in correlated flux), the residuals from the best-fit linear motion are likely to be dominated by the internal structure of the maser spots, rather than the thermal noise. In fact, adopting the distance of 2.8 kpc (see next subsection for distance determination), the mean values of δ_X and δ_Y correspond to 0.06 AU and 0.08 AU. Observations of other H_2O maser sources suggested that maser clouds have internal structure with a typical scale of 1 AU and a typical velocity width of $0.5\,{\rm km\,s^{-1}}$ (e.g., Gwinn 1994). Assuming the same values for masers in OH 43.8−0.1, one can roughly estimate possible changes in the maser peak positions due to internal turbulent motions during our time span

Table 1. Results of proper motion measurements.

ID*	V_{LSR}†	X‡	Y‡	μ_X§	μ_Y§	Epochs‖	δ_X#	δ_Y#
1	50.92	−145.105	136.124	0.129	0.152	00111	0.012	0.027
2	50.47	−145.085	136.030	0.088	0.416	11111	0.028	0.035
3	50.04	−145.132	136.030	0.202	0.461	11111	0.031	0.026
4	49.62	−145.117	135.997	0.180	0.529	11111	0.030	0.028
5	49.20	−145.102	135.982	0.180	0.552	11111	0.017	0.030
6	48.78	−145.092	135.961	0.146	0.689	11111	0.016	0.024
7	48.36	−145.089	135.957	0.146	0.740	11111	0.021	0.016
8	47.94	−145.093	135.998	0.144	0.699	11111	0.020	0.036
9	47.52	−145.084	136.015	0.140	0.647	11111	0.015	0.022
10	47.10	−145.076	136.030	0.166	0.570	11111	0.011	0.023
11	46.67	−145.090	136.040	0.197	0.518	11111	0.026	0.039
12	46.29	−155.368	134.127	0.088	0.325	10101	0.035	0.029
13	45.02	−82.968	−276.683	−0.011	0.204	00111	0.000	0.058
14	44.99	−267.836	−507.013	0.113	−0.212	11101	0.033	0.069
15	44.56	−82.884	−276.457	−0.159	−0.229	01111	0.031	0.066
16	44.15	−82.811	−276.482	−0.281	−0.279	11111	0.031	0.047
17	43.72	−82.815	−276.430	−0.286	−0.509	11111	0.021	0.053
18	43.29	−82.809	−276.490	−0.245	0.037	11100	0.042	0.019
19	42.87	−155.561	134.052	0.562	0.391	11100	0.004	0.064
20	42.49	−218.197	104.703	−0.117	−0.039	00111	0.017	0.006
21	42.07	−218.168	104.679	−0.181	0.022	00111	0.005	0.002
22	41.65	−218.141	104.652	−0.264	0.103	00111	0.007	0.012
23	41.62	−271.528	−48.440	−0.097	−0.117	11111	0.023	0.032
24	41.20	128.780	−809.712	0.454	−0.599	11111	0.042	0.078
25	40.76	−215.215	106.730	0.131	0.014	11100	0.020	0.016
26	40.38	−75.557	73.994	0.221	0.100	00111	0.049	0.011
27	40.23	398.851	−106.395	0.553	−0.164	01111	0.008	0.082
28	39.96	−51.367	44.381	0.102	0.176	00111	0.017	0.008
29	39.96	−18.276	−310.044	−0.297	−0.056	00111	0.028	0.012
30	39.51	−51.386	44.441	0.163	0.116	11111	0.010	0.022
31	39.51	−18.438	−310.014	−0.127	−0.103	11111	0.006	0.015
32	39.09	−18.481	−310.026	−0.018	−0.104	11111	0.013	0.010
33	38.66	−18.555	−309.907	0.130	−0.297	01111	0.010	0.014
34	38.66	−0.008	0.022	0.004	−0.078	11110	0.003	0.006
35	38.25	0.000	0.000	0.000	0.000	11111	0.000	0.000
36	37.85	−65.069	−250.810	−0.046	−0.317	00111	0.010	0.005
37	37.81	−0.023	0.029	0.025	−0.017	11100	0.019	0.009
38	37.40	−65.013	−250.881	−0.128	−0.094	11101	0.001	0.048
39	36.13	−52.904	−249.517	0.822	−0.185	11110	0.047	0.024
40	35.72	−52.870	−249.514	0.809	−0.218	11111	0.054	0.040
41	35.30	−52.734	−249.572	0.576	−0.064	11111	0.048	0.032
42	34.88	−52.602	−249.609	0.392	−0.012	11111	0.034	0.024
43	34.44	−52.616	−249.555	0.443	−0.058	00111	0.060	0.023

* Spot ID number.
† LSR velocity in $km\,s^{-1}$ (averaged over detected epochs).
‡ Best-fit positions at the first epoch in mas (extrapolated for those not detected at the first epoch).
§ Best-fit proper motions (in $mas\,yr^{-1}$).
‖ Detected epochs: '1' for detection, and '0' for non-detection.
RMS position residuals from the best-fit proper motions (in mas).

of observations (281 days) as $0.5\,km\,s^{-1} \times 281 \times 86400\,s = 0.08\,AU$, which is quite close to the physical scales given by the mean values of δ_X and δ_Y.

The proper-motion vectors of maser spots listed in table 1 are shown in figure 2a. Proper motion vectors are shown for the spots with proper motions greater than $0.1\,mas\,yr^{-1}$ (40 among the 43 spots in table 1). As described in the previous section, the maser spot at $38.2\,km\,s^{-1}$ was taken to be a reference spot, and thus all of the proper-motion vectors are relative to the proper motion of the reference spot, itself. The proper

motion of the reference maser spot could not be measured in the present study, and thus it might introduce a bias to the proper motions of other maser spots if the reference maser spot, itself, has a large proper motion. However, the mean values of μ_X and μ_Y for 43 spots in table 1 are 0.117 mas yr^{-1} and 0.086 mas yr^{-1}, corresponding to 1.6 km s^{-1} and 1.1 km s^{-1} at a source distance of 2.8 kpc. These values of the mean proper motions are fairly smaller than the radial velocity width ($\sim$ 30 km s^{-1}, see figure 1) and the mean size of the proper motion vectors in the north–south bipolar flow (0.6 mas yr^{-1}, see below), indicating that the proper motion of the reference maser spot does not introduce large systematic motions of the reference frame in figure 2.

As can be seen in figure 2a, the global distribution of the proper motions show a bipolar structure with red-shifted northern components around $(X, Y) = (-145, 136)$ moving toward the north, and a moderately blue-shifted southern component at $(129, -810)$ moving toward the south. The mean size of the proper-motion vectors for these spots (spot number 1 to 11, and 24 in table 1) is 0.58 mas yr^{-1} (corresponding to 7.7 km s^{-1} at a distance of 2.8 kpc), which gives a measure of the outflow velocity. Note that while there are more than 10 spots in the red-shifted northern components, there is only one blue-shifted southern component for which the proper motion was measured. This is likely to be due to the geometric effect of bipolar flow, which causes the difference in the column density of masing gas toward these components: red-shifted components locate on the far side of the protostar along the line-of-sight, and thus the column density of masing gas is higher than the blue-shifted components, which locate on the near side of the protostar. Between these two components there is a cluster of maser spots with X between -80 mas and -20 mas and Y between -310 mas and -250 mas, which hereafter we refer to as the 'central cluster', shown in figure 2c. The directions and amplitudes of proper-motion vectors in the central cluster are quite different from those of the northern and southern components, showing rather complex structures. For instance, the maser features at $(X, Y) = (-83, -276)$ (spot number 13, 15 to 18 in table 1) and at $(-18, -310)$ (spot number 29, 31 to 33) exhibit large velocity changes within the maser features in 0.3 mas scale ($\sim$ 0.8 AU). Highly blue-shifted maser spots at a radial velocity of 25 to 34 km s^{-1} (which were detected only for DOY 120, 2004) also locate in the central cluster area (open circles in figure 2c). These complex structures of the central cluster may indicate that the protostar is associated with the central cluster, and the protostar's activity causes the complexity.

In contrast to an expanding shell, such as those found in Cep A R5 (Torrelles et al. 2001) or W 75N VLA2 (Torrelles et al. 2003), the proper motions in the shell-like structure found by Downes et al. (1979) cannot be represented by a coherent expansion from the shell center. The proper motions of the 'shell' in the north–south direction are 0.5 to 0.7 mas yr^{-1}, and are much larger than those of the east–west direction, which are around 0.1 to 0.2 mas yr^{-1}. The global properties of the proper-motion distributions indicate that the structure of the OH 43.8$-$0.1 H_2O masers can be represented by bipolar flow plus a central cluster, and that the shell-like structure in figure 2b is just a part of bipolar flow and the central cluster (for further discussion on the structure of OH 43.8$-$0.1, see the next section).

3.4. Distance Determinations by Statistical Parallax

The distances to maser sources can be determined from the dispersions of the radial velocities and the proper motions based on statistical parallax. Statistical parallax assumes only that the velocity dispersions are isotropic, and the basic equation for distance determinations with statistical parallax can be written as

$$D = \frac{\sigma_V}{\sigma_\mu} \equiv \frac{\sigma_V}{\sqrt{(\sigma_{\mu X}^2 + \sigma_{\mu Y}^2)/2}}. \quad (1)$$

Here, D is the source distance, σ_V the radial velocity dispersion, and σ_μ the one-dimensional proper motion dispersion; $\sigma_{\mu X}$ and $\sigma_{\mu Y}$ are the proper-motion dispersions in the X and Y directions, respectively. In practice, however, equation (1) is too much simplified, and one has to take into account the effect of observational uncertainties using the following equation instead of equation (1):

$$D = \frac{\sigma'_V}{\sigma'_\mu} \equiv \frac{\sqrt{\sigma_V^2 - \epsilon_V^2}}{\sqrt{\left[(\sigma_{\mu X}^2 - \epsilon_X^2) + (\sigma_{\mu Y}^2 - \epsilon_Y^2)\right]/2}}. \quad (2)$$

The ϵ terms correct for the effect of the observational uncertainties, which broadens the widths of the velocity and the proper motion. In the following analyses we make use of equation (2) as the basic equation for distance determination based on statistic parallax [but note that equations (1) and (2) give almost identical results, because the ϵ terms are sufficiently small in the present study].

In several cases, H_2O maser sources show bipolarity, and thus anisotropy. Therefore, careful analyses are necessary to obtain reliable distances. In the present work, we performed statistical parallax analyses based on four different definitions of $\sigma_{\mu X}$ and $\sigma_{\mu Y}$: (i) using all maser spots, with dispersion σ, defined as the root-mean-square value from the average [i.e., $\sigma_{\mu X} = \sqrt{\sum(\overline{\mu}_X - \mu_{X,i})^2/N}$], (ii) using all maser spots, with dispersion σ, defined as the peak-to-peak value [i.e., $\sigma_{\mu X} = \max(\mu_{Xi}) - \min(\mu_{Xi})$], (iii) the same definition of σ in (i), but only with spots in the central cluster, and (iv) the same definition of σ in (ii), but only with spots in the central cluster. Note that in all cases, the dispersions of the LSR velocities are also defined in the same manner as those of the proper motions [i.e., $\sigma_V = \sqrt{\sum(\overline{V} - V_i)^2/N}$ for cases (i) and (iii), and $\sigma_V = \max(V_i) - \min(V_i)$ for cases (ii) and (iv)]. Cases (iii) and (iv) are to avoid the anisotropy caused by the bipolarity of the maser flow: as already seen in the previous sections, while the large scale proper motions are represented by a bipolar flow, the proper motions in the central cluster show a rather complex structure. Also, cases (ii) and (iv) are for testing how different definitions of 'dispersion' would affect the results, since the distributions of the LSR velocities and the proper motions are not necessarily modeled by a Gaussian distribution. In all cases, ϵ_V is taken to be 0.21 km s^{-1}, which is half of the velocity resolution and the threshold for identifying maser spots in different epochs; ϵ_X and ϵ_Y are taken to be 0.029 and 0.038 mas yr^{-1}, which are determined from the averaged

Table 2. Results of distance determinations.

Case	Spot*	$N^\dagger$	def $\sigma^\ddagger$	$\sigma'_V{}^\S$	$\sigma'_\mu{}^\parallel$	$D^\#$
i	all	43	RMS	4.69	0.303	3.28
ii	all	43	PP	16.5	1.23	2.82
iii	CC	16	RMS	3.72	0.294	2.67
iv	CC	16	PP	10.1	0.930	2.30
					Mean	2.8 ± 0.5

* Spot selection: all for all spots, and CC for spots in the central cluster.
† Number of spots used in analyses.
‡ Definitions for σ_V, $\sigma_{\mu X}$, and $\sigma_{\mu Y}$: RMS for root-mean-square, and PP for peak-to-peak definitions, see text.
§ σ'_V in $\mathrm{km\,s^{-1}}$ [equation (2)].
‖ σ'_μ in $\mathrm{mas\,yr^{-1}}$ [equation (2)].
Determined distance in kpc.

values of δ_X and δ_Y and the time span $\tau = 281\,\mathrm{d} = 0.77\,\mathrm{yr}$, as $\epsilon_X = \overline{\delta}_X/\tau$ and $\epsilon_Y = \overline{\delta}_Y/\tau$.

Table 2 summarizes the results of distance determinations with cases (i) to (iv). The calculated distances vary from 3.3 kpc for case (i) to 2.3 kpc for case (iv). There are also some systematic trends in 4 cases: analyses with all spots tend to give larger distances, and analyses with the RMS definition of the dispersions tend to give larger distances. The former tendency may reflect a geometric effect of bipolarity. For instance, in cases (i) and (iii) the dispersions of the proper motions are similar, but the dispersions of the LSR velocities are increased by a factor of 1.26 when all spots are included [case (i)], yielding a further distance. This result may imply that the location of the bipolar structure is head-on, i.e., the angle between the bipolar axis and the line-of-sight is less than 45°. The origin of the latter tendency in table 2 (larger distance for RMS definition of dispersions) is unclear, but the difference of the distances for two definitions of σ is a factor of 1.14, which could be an error introduced by the small-number statistics ($N = 16$ or 43).

It is not easy to judge which of the four cases best represents the true distance to OH 43.8−0.1, since all four cases have advantages and disadvantages. While analyses with spots only in the central cluster avoid the effect of bipolarity, the number of spots becomes smaller, which degrades the statistic reliability. The peak-to-peak definition of dispersions is severely affected by an outlier with an extreme LSR velocity or proper motions (if exists), while the RMS definitions of dispersions may not work well for non-Gaussian distributions (e.g., V_{LSR} distribution in figure 1). In order to obtain the most-likely value of the distance to OH 43.8−0.1, here we conservatively take an average of 4 cases, which yields $D = 2.8 \pm 0.5$ kpc. This distance is consistent with the near kinematics distance (~ 3 kpc), and rules out the far kinematic distance (~ 9 kpc).

4. Discussion

4.1. Structure of OH 43.8−0.1 H_2O Masers

The key to understanding the structure and kinematics of the H_2O masers in the context of star formation in OH 43.8−0.1 is to know the location of the forming star relative to the maser spots in figure 2. Unfortunately, H_2O maser spots are most likely to be located in shock regions where the outflow from a forming star hits ambient gases, and thus the position of the forming star cannot be directly obtained from H_2O maser observations. An approach to obtain the position of a forming star is to use the continuum radio emissions, since a forming OB star radiates strong UV photons, and produces a compact H II region. In fact, an Ultra-Compact H II region (UC H II) was found by VLA observations at frequencies of 8 GHz and 15 GHz (Kurtz et al. 1994). They found an unresolved UC H II at the position of $(\alpha_{\mathrm{J2000}}, \delta_{\mathrm{J2000}}) = (19^{\mathrm{h}}11^{\mathrm{m}}53\overset{\mathrm{s}}{.}987, +09°35'50\overset{''}{.}308)$ with an uncertainty of $0\overset{''}{.}1$. This agrees well with our absolute position determination for the reference spot, $(19^{\mathrm{h}}11^{\mathrm{m}}53\overset{\mathrm{s}}{.}986, +09°35'50\overset{''}{.}22) \pm 0\overset{''}{.}2$. Thus, the UC H II regions indeed locate in the maser emitting regions, but the precise location in figure 2a is still unclear due to the position error.

As for OH maser emissions, Argon et al. (2000) located OH maser spots with respect to the UC H II region using the VLA A-Array. Their results demonstrated the clear association of the OH masers with the UC H II region. It is notable that the LSR velocity of OH maser emissions ranges from 40 to $45\,\mathrm{km\,s^{-1}}$ (Argon et al. 2000), which is fairly close to the LSR velocity range of the central cluster shown in figure 2c (34 to $45\,\mathrm{km\,s^{-1}}$). The results of OH maser observations by Argon et al. (2000) may imply a connection between the OH masers and the central cluster of the H_2O masers, and thus the possible link between the central cluster and the UC H II region.

In addition to the OH masers, methanol (CH_3OH) masers at 6.7 GHz were found in OH 43.8−0.1 (Menten 1991; Szymczak et al. 2000). The 6.7 GHz methanol maser is categorized as a class II methanol maser, which shows a clear connection with star formation, presumably associated with accreting matter or an accretion disk around a protostar. Menten (1991) reported that the methanol maser line in OH 43.8−0.1 has a V_{LSR} range of 39 to $44\,\mathrm{km\,s^{-1}}$. Szymczak et al. (2000) also confirmed this result, while their results show that the peak intensity occurs at 39 to $40\,\mathrm{km\,s^{-1}}$. These V_{LSR} ranges are closer to those of the central cluster (34 to $45\,\mathrm{km\,s^{-1}}$), rather than northern maser spots at $(X, Y) = (-145, 136)$ (47 to $51\,\mathrm{km\,s^{-1}}$). Thus, a simple interpretation of V_{LSR} of methanol maser lines is that methanol maser emissions are associated with the central cluster. If these methanol emissions are indeed associated with a forming star, and thus UC H II, this indicates that the unresolved UC H II is located in or near the central cluster.

Another way to estimate the position of a forming star with respect to the maser features is to use kinematic information. Since the outflow is powered by the forming star, its position can be estimated as an origin of outflow motion. Detailed modeling has been done for several sources to evaluate the position of the outflow origin as well as distances (e.g., Reid et al. 1988; Gwinn et al. 1992; Imai et al. 2000). Here, we take one of the simplest (and often used) kinematic models, which assumes a radial outflow from a single origin with a constant outflow velocity. The basic technique is essentially the same as that used in Imai et al. (2000), where the outflow origin was determined to minimize the differences between the observed velocity vectors and the model velocity vectors. Based on this kinematic modeling, the outflow origin was estimated to be at $(X, Y) = (-260 \pm 130, -250 \pm 130)$. Although the error

bars are relatively large, the estimated position of the outflow origin coincides with the position of the central cluster within the error bars. Considering the discussions described above, one can infer that the central maser cluster is associated with a forming star, and the bipolar flow in the north–south direction is powered by the forming star in or near the central cluster. This kind of structure, a bipolar flow plus a central cluster, is also seen in other H_2O maser sources, such as IRAS 05413−0104 (Claussen et al. 1998) and IRAS 21391+5802 (Patel et al. 2000), which are low-mass star-forming regions. To obtain more firm conclusions on the case for OH 43.8−0.1, a precise collocation of H_2O maser spots with UC H II regions is definitely required.

The distance to OH 43.8−0.1 provide a physical scale of H_2O emitting regions. The north–south bipolar extension (0.″98) corresponds to a physical scale of 2740 AU at a distance of 2.8 kpc. This scale is remarkably smaller than the maser structures of other massive star-forming regions, such as W 49N (∼ 20000 AU, Gwinn et al. 1992), Sgr B2 (∼ 28000 AU, Reid et al. 1988), and Orion KL (∼ 19000 AU, Genzel et al. 1981a). The size difference mainly originates from the small outflow velocity of OH 43.8−0.1, rather than age differences in these star-forming regions. In fact, a dynamical age estimate of the OH 43.8−0.1 H_2O masers gives $\tau_{\rm dyn} = 750 \pm 100$ yr for the north–south bipolar extension, which is not much different from those of massive star-forming regions, for instance, $\tau_{\rm dyn} \sim 500$ for W 49N (Gwinn et al.1992). On the other hand, the H_2O maser motion in these massive star-forming regions exceeds 100 km s^{-1}, while that in OH 43.8−0.1 is ∼ 8 km s^{-1}. Thus, this scale difference reflects the difference of outflow energy between OH 43.8−0.1 and other massive star-forming regions; this is presumably linked to lower power, implying a lower mass of the forming star in OH 43.8−0.1 than the protostars in W 49N, Sgr B2, and Orion KL.

4.2. *Constraints on Galactic Rotation Curve*

Although this study presents a distance measurement of only one source, the result can be used to constrain the rotation properties of the Galaxy. Assuming a circular rotation at any radius of the Galaxy, the observed LSR velocity can be written as

$$V_{\rm LSR} = \left[\Theta(R)\left(\frac{R_0}{R}\right) - \Theta_0\right]\sin l. \quad (3)$$

Here, R and R_0 are the galacto-centric distances of the source (OH 43.8−0.1 for the present study) and the Sun, $\Theta(R)$ and Θ_0 are the circular rotation speed of the Galaxy at the radius of the source and the Sun, and l is the galactic longitude. Note that $V_{\rm LSR}$ and l are observables, and R can also be regarded as an observable, because R is written as

$$R = \sqrt{D^2 + R_0^2 - 2DR_0\cos l}. \quad (4)$$

Hence, one can immediately know R once D and R_0 are given. Equation (3) contains three parameters to be determined, namely, R_0, Θ_0, $\Theta(R)$. Among them, the galactic constants, R_0 and Θ_0, are not necessarily unknown as there have been numerous studies to evaluate them. Therefore, if R_0 and Θ_0 are given, then $\Theta(R)$ can be determined, giving a constraint on the galactic rotation speed.

The IAU standard values are $R_0 = 8.5$ kpc and $\Theta_0 = 220$ km s^{-1} (Kerr, Lynden-Bell 1986), but several recent studies claim different values. Determinations of R_0 later than 1986 tend to give smaller values; Reid (1993) summarized the determinations of R_0, giving $R_0 = 8.0 \pm 0.5$ kpc. As for Θ_0, the situation is very complicated: while number of recent studies with various methods gave values of around 200–220 km s^{-1}, being in good agreement with previous ones (e.g., Mignard 2000; Bedin et al. 2003; Kalirai et al. 2004; Reid, Brunthaler 2004), there were also some studies which report fairly smaller, or larger, values varying from 180 to 270 km s^{-1} (e.g., Olling, Merrifield 1998; Miyamoto, Zhu 1998). In the following analyses, we conservatively take large errors for both R_0 and Θ_0, taking $R_0 = 8.0 \pm 1.0$ kpc and $\Theta_0 = 220 \pm 50$ km s^{-1}.

Here, we rewrite equation (3) by introducing a new parameter, $\theta_r \equiv \Theta(R)/\Theta_0$, as

$$\theta_r = \left(\frac{V_{\rm LSR}}{\Theta_0 \sin l} + 1\right)\frac{R}{R_0}. \quad (5)$$

Based on the galactic constants, R_0 and Θ_0, one can determine θ_r, which is the ratio of the galactic rotation speeds at the source and at the Sun. If the rotation curve is completely flat, as found in many bright spiral galaxies (e.g., Sofue, Rubin 2001), θ_r should be unity. In order to obtain θ_r from equation (5), one also has to know the value of $V_{\rm LSR}$, the LSR velocity. Assuming that the central cluster of the H_2O masers is indeed associated with the UC H II regions, and thus its radial velocity reflects the systematic velocity of OH 43.8−0.1, the averaged velocity gives $V_{\rm LSR} = 40$ km s^{-1}. Observations of molecular gases with CS and CO lines give $V_{\rm LSR} = 43$–44 km s^{-1} (Plume et al. 1992; Shepherd, Churchwell 1996), and methanol maser lines and OH maser lines lie in the LSR velocity range of 39 to 44 km s^{-1} (Menten 1991; Szymczak et al. 2000; Argon et al. 2000). Summarizing these results, here we adopt $V_{\rm LSR} = 42 \pm 3$ km s^{-1} as the systemic velocity of OH 43.8−0.1. Using these values ($R_0 = 8.0 \pm 1.0$ kpc, $\Theta_0 = 220 \pm 50$ km s^{-1}, $D = 2.8 \pm 0.5$ kpc, and $V_{\rm LSR} = 42 \pm 3$ km s^{-1}), equation (5) yields

$$\theta_r = 1.00^{+0.10}_{-0.06}, \quad (6)$$

where the upper and lower limits are calculated as the worst values with possible combinations of the above mentioned parameter ranges. The value of θ_r indicates that there is no systematic difference between the rotation speeds at OH 43.8−0.1 and at the Sun, and thus that the galactic rotation curve is fairly flat, being consistent with previous studies (e.g., Honma, Sofue 1997). For $R_0 = 8.0$ kpc, equation (4) gives $R = 6.3$ kpc as a galacto-centric distance of OH 43.8−0.1, and the interpolation of the rotation speed between the Sun and OH 43.8−0.1 suggests that the flat rotation curve spans nearly 2 kpc.

5. Summary and Concluding Remark

We carried out 5-epoch observations of the OH 43.8−0.1 H_2O masers with VERA, and successfully measured the proper motions of OH 43.8−0.1 H_2O masers for the first time. The large-scale maser map revealed a north–south extension of the maser spots, and proper-motion measurements showed that the distribution as well as the kinematics of the OH 43.8−0.1 H_2O

masers can be represented by bipolar flow in the north–south direction plus the central cluster, which has a rather complex velocity structure. Based on the statistical parallax, we also determined the distance to OH 43.8−0.1 as 2.8 ± 0.5 kpc, ruling out a far kinematic distance. The distance, combined with previous studies on the galactic constants, such as R_0 and Θ_0, gave a constraint on the flatness of galactic rotation curve, showing no systematic difference in the galactic rotation velocity at the Sun and OH 43.8−0.1.

In the near future, VERA will observe hundreds of H_2O maser sources to perform the astrometry of galactic star-forming regions. While the main target of VERA is to investigate the structure and dynamics of the Milky Way Galaxy via astrometry of maser sources, VERA will also provide useful information on the internal structures and kinematics of star-forming regions; the present study is one of the first examples of such valuable by-products of VERA.

One of the authors (MH) acknowledges financial support from Inamori Foundation and from a grant-in-aid (No. 16740120) from the Ministry of Education, Culture, Sports, Science and Technology (MEXT). Part of the data reduction was performed at the Astronomical Data Analysis Center (ADAC) of the NAOJ, which is an inter-university research institute of astronomy operated by MEXT.

References

Alcolea, J., Menten, K. M., Moran, J. M., & Reid, M. J. 1993, in Astrophysical Masers, Lecture Note in Physics 412, ed. A. W. Clegg & G. E. Nedoluha (Berlin: Springer), 225
Argon, A. L., Reid, M. J., & Menten, K. M. 2000, ApJS, 129, 159
Bedin, L. R., Piotto, G., King, I. R., & Anderson, J. 2003, AJ, 126, 247
Claussen, M. J., Marvel, K. B., Wootten, A., & Wilking, B. A. 1998, ApJ, 507, L79
Dickinson, D. F., Blair, G. N., Davis, J. H., & Cohen, N. L. 1978, AJ, 83, 32
Downes, D., Genzel, R., Moran, J. M., Johnston, K. J., Matveyenko, L. I., Kogan, L. R., Kostenko, V. I., & Rönnäng, B. 1979, A&A, 79, 233
Furuya, R. S., Kitamura, Y., Wootten, H. A., Claussen, M. J., & Kawabe, R. 2005, A&A in press
Furuya, R. S., Kitamura, Y., Wootten, H. A., Claussen, M. J., Saito, M., Marvel, K. B., & Kawabe, R. 2000, ApJ, 542, L135
Genzel, R., et al. 1981b, ApJ, 247, 1039
Genzel, R., & Downes, D. 1977, A&AS, 30, 145
Genzel, R., Reid, M. J., Moran, J. M., & Downes, D. 1981a, ApJ, 244, 884
Goddi, C., Moscadelli, L., Alef, W., & Brand, J. 2004, A&A, 420, 929
Gwinn, C. R. 1994, ApJ, 429, 253
Gwinn, C. R., Moran, J. M., & Reid, M. J. 1992, ApJ, 393, 149
Honma, M., et al. 2003, PASJ, 55, L57
Honma, M., et al. 2004, PASJ, 56, L15
Honma, M., Kawaguchi, N., & Sasao, T. 2000, in Proc. SPIE, 4015, Radio Telescope, ed. H. R. Buthcer (Washinton: SPIE), 624
Honma, M., & Sofue, Y. 1997, PASJ, 49, 453
Imai, H., Kameya, O., Sasao, T., Miyoshi, M., Deguchi, S., Horiuchi, S., & Asaki, Y. 2000, ApJ, 538, 751
Imai, H., Watanabe, T., Omodaka, T., Nishio, M., Kameya, O., Miyaji, T., & Nakajima, J. 2002, PASJ, 54, 741
Kalirai, J. S., et al. 2004, ApJ, 601, 277
Kerr, F. J., & Lynden-Bell, D. 1986, MNRAS, 221, 1023
Kobayashi, H., et al. 2003, in ASP Conf. Ser. 306, New Technologies in VLBI, ed. Y. C. Minh (San Francisco: ASP), 367
Kurtz, S., Churchwell, E., & Wood, D. O. S. 1994, ApJS, 91, 659
Lekht, E. E. 2000, A&AS, 141, 185
Menten, K. M. 1991, ApJ, 380, L75
Mignard, F. 2000, A&A, 354, 522
Miyamoto, M., & Zhu, Z. 1998, AJ, 115, 1483
Olling, R. P., & Merrifield, M. R. 1998, MNRAS, 297, 943
Patel, N. A., Greenhill, L. J., Herrnstein, J., Zhang, Q., Moran, J. M., Ho, P. T. P., & Goldsmith, P. F. 2000, ApJ, 538, 268
Plume, R., Jaffe, D. T., & Evans, N. J., II 1992, ApJS, 78, 505
Reid, M. J. 1993, ARA&A, 31, 345
Reid, M. J., & Brunthaler, A. 2004, ApJ, 616, 872
Reid, M. J., Schneps, M. H., Moran, J. M., Gwinn, C. R., Genzel, R., Downes, D., & Rönnäng, B. 1988, ApJ, 330, 809
Schneps, M. H., Lane, A. P., Downes, D., Moran, J. M., Genzel, R., & Reid, M. J. 1981, ApJ, 249, 124
Seth, A. C., Greenhill, L. J., & Holder, B. P. 2002, ApJ, 581, 325
Shepherd, D. S., & Churchwell, E. 1996, ApJ, 457, 267
Sofue, Y., & Rubin, V. 2001, ARA&A, 39, 137
Szymczak, M., Hrynek, G., & Kus, A. J. 2000, A&AS, 143, 269
Torrelles, J. M., et al. 2001, Nature, 411, 277
Torrelles, J. M., et al. 2003, ApJ, 598, L115